

its intrinsic magnetic exchange interaction and spin-orbit coupling (SOC) effect, giving birth to the ferrovalley concept. Moreover, coexisting ferroelectric and ferrovalley polarizations in bilayer stacked VSi_2P_4 , FeCl_2 , and RuBr_2 with interlayer antiferromagnetic (AFM) coupling are found [10]. The high-temperature superconducting property of monolayer CoSb has been investigated in detail by first-principles calculations [11]. Interestingly, intrinsic quantum anomalous Hall effect (QAHE) is theoretically predicted and experimentally proved in topological insulators with magnetic doping [12], and intrinsic magnetic topological 2D MnBi_2Te_4 materials [13–15]. In addition, the odd-even-layer-dependent QAH and quantum spin Hall effects are demonstrated in 2D LiFeTe topological insulators [16]. Thus, 2D magnetic materials provide a suitable platform for investing novel states of matter and have become one of the hot spots for research.

For magnetic materials, the magnetization direction has a decisive impact on their physical properties because of their correlation with the symmetry and spin states of a system [17, 18]. The electric resistance value depends on the direction of magnetization in FM metals at saturation [19]. There is a cosine function dependence between valley polarization and magnetization direction in 2D valley materials [20–25]. Due to the coupling of magnetic and topological states, the topological gap of QAH insulator monolayer can be effectively adjusted by regulating the magnetization direction by using an external magnetic field [26]. In addition, under the influence of an external magnetic field in different directions, the spin states can be redirected [27]. Several studies have demonstrated the theoretical feasibility of achieving different topological states by regulating the magnetization direction in different Chern insulators, e.g., by tuning the magnetization direction, the systems can vary from a Weyl semimetal to a QAH insulator [28]. Furthermore, the Chern number C in topological insulators can be effectively regulated via manipulating the magnetization direction of system, which provides a novel way to acquire higher Chern number [29–33]. Specially, QAHE with adjustable Chern number based on metal-oxide lattice systems have been extensively studied [34–37]. Therefore, it will be interesting and meaningful to explore other novel physical states of matter in 2D magnetic materials by adjusting its magnetization direction through external magnetic field.

In this study, the magnetic, electronic, and topological properties of the monolayer XBiO_3 ($X = \text{Pd}, \text{Pt}$) are investigated. The monolayer XBiO_3 presents a FM coupling with in-plane magnetic anisotropy. The Berezinskii–Kosterlitz–Thouless transition temperatures of monolayers PdBiO_3 and PtBiO_3 are 432 and 550 K, respectively. Interestingly, monolayer XBiO_3 presents a topological phase transition behavior dependent on the magnetization direction. When the magnetization direction

changes in the xy plane, monolayer XBiO_3 switch between QAH insulator with $C = |1|$ and topological trivial semimetal with a period of 60° . It is caused by the breaking or protecting mirror symmetries for different polar angle Ψ . Comparatively, as the magnetization direction alters in the xz plane, monolayer XBiO_3 vary among QAH insulator with $C = |3|$, QAH insulator with $C = |1|$ as well as mixed semimetal and QAH state with a period of 180° . Therefore, the Chern number of monolayer XBiO_3 can be regulated by changing the magnetization direction. The topological band gaps of monolayers PdBiO_3 and PtBiO_3 can reach to 114 and 132 meV, respectively. Notably, the QAH feature is robust for strain and different U values. This work presents two promising materials for practical implementation of spintronics devices.

2 Computational details

We employ the methodology of first-principles calculations, as implemented in the Vienna *ab initio* Simulation Package (VASP), based on density-functional theory (DFT) [38]. The projector-augmented-wave (PAW) potential [39] is utilized, with the exchange-correlation functional treated by generalized gradient approximation (GGA) using the Perdew–Burke–Ernzerhof (PBE) functional [40]. The plane-wave basis is employed with a kinetic energy cut-off of 500 eV. The convergence criteria for energy and force are set at 10^{-7} eV and 10^{-3} eV/Å, respectively. In order to obtain a more realistic electronic structure, SOC effect is also taken into account in the calculation. The Brillouin zone is sampled using a $15 \times 15 \times 1$ Γ -centered Monkhorst-Pack grid for accurate representation. The PBE+ U method is used to treat the d orbitals, U is set to be 3.0 and 4.0 eV for Pd and Pt, respectively [41]. To confirm the results, the calculations are also checked using the Heyd–Scuseria–Ernzerhof (HSE06) method. To avoid the influence between adjacent layers, a vacuum layer in the z direction with a thickness of 18 Å is applied. The phonon spectrum is obtained by the PHONOPY code based on the density functional perturbation theory using a $4 \times 4 \times 1$ supercell [42]. *Ab initio* molecular dynamics (AIMD) simulations are adopted using a Nosé–Hoover thermostat to control the system temperature with an NVT ensemble [43]. The VASPKIT package is used to process the calculation data [44]. A maximized localization function is created using the Wannier90 package [45], where the d orbitals of Pd/Pt atom and p orbitals of Bi and O atoms are considered as the projected orbitals for monolayer XBiO_3 ($X = \text{Pd}, \text{Pt}$). The AHC for monolayer XBiO_3 is evaluated by taking a very dense k -point mesh of $500 \times 500 \times 1$ in the Brillouin zone. The edge states are calculated by using the WannierTools software package [46].

3 Results and discussion

3.1 Crystal structure and magnetic property

Figure 1(a) shows the crystal structure of monolayer (ML) $X\text{BiO}_3$ ($X = \text{Pd}, \text{Pt}$) with a space group of $P\bar{3}1m$, in which the middle layer Pd/Pt atoms are sandwiched by two layers of O atoms, leaving the Bi atoms on the outmost side. Figure 1(b) displays the first Brillouin zone with high symmetry points of ML $X\text{BiO}_3$. Notably, three orange vertical mirror planes are presented, corresponding to the C_3 rotation symmetry. The optimized lattice constants are 5.36 and 5.44 Å for ML PdBiO_3 and PtBiO_3 , respectively, as presented in Table S1. The calculated energy difference between FM and three AFM configurations ($\Delta E = E_{\text{Néel/Stripe/Zigzag}} - E_{\text{FM}}$) are 0.12, 0.43, and 0.18 eV for ML PdBiO_3 and 0.04, 0.44, and 0.26 eV for ML PtBiO_3 , respectively, indicating the FM coupling of ML $X\text{BiO}_3$. The calculated magnetic moment is $2 \mu_{\text{B}}/\text{f.u.}$. The binding energy of ML $X\text{BiO}_3$ is computed as the energy difference between ML $X\text{BiO}_3$ and the Ni, Bi crystal, and O molecule, given by $E_{\text{b}} = E(X\text{BiO}_3) - E(X) - E(\text{Bi}) - 3/2E(\text{O}_2)$. The obtained formation energies of -2.98 and -2.92 eV implies that the ML PdBiO_3 and PtBiO_3 are energetically stable and its experimental synthesis is achievable, as shown in Table S1. The dynamical and thermal stabilities of ML $X\text{BiO}_3$ is indicated by study their phonon dispersion spectrums and AIMD simulations, as depicted in Figs. S1(a)–(d). The absence of imaginary frequencies in the phonon spectra confirms the dynamical stability of the material. During the AIMD simulations, the total energy fluctuates within a small range, the structure of ML $X\text{BiO}_3$ remains intact, indicating its thermal stability. Moreover, the elastic constants C_{11}, C_{22}, C_{12} and C_{66} of ML $X\text{BiO}_3$ (see Table S2), which fulfill the Born criteria conditions $C_{11}, C_{22}, C_{66} > 0; C_{11}C_{22} - C_{12}^2 > 0$, confirming the mechanical stability of ML $X\text{BiO}_3$ [47]. Figures S2(a) and (b) plot the electron localization function of ML $X\text{BiO}_3$. Notably, there are significant electron localization around the Bi and O atoms, suggesting an ionic bonding between X and Bi (O) atoms. During the forming of ML $X\text{BiO}_3$, the Pd/Pt and Bi atoms will contribute six electrons to the three O atoms, remaining seven valence electrons in the d orbitals of Pd/Pt atom. The Pd-Pd/Pt-Pt and Pd-O/Pt-O bond lengths are 3.09/3.14 and 2.09/2.10 Å, respectively.

Due to the localization of d orbitals of Pd/Pt, the direct-exchange should be weaker than the super-exchange [48]. The Pd/Pt atom in ML $X\text{BiO}_3$ is surrounded by six O atoms, forming a distorted octahedra [49, 50]. Under this crystal field, the d orbitals of Pd/Pt atom are split into a_{g} (d_{z^2}), $e_{\text{g}1}$ ($d_{xy}, d_{x^2-y^2}$) and $e_{\text{g}2}$ (d_{xz}, d_{yz}) orbitals. The seven electrons first fill the a_{g} (d_{z^2}), $e_{\text{g}1}$ ($d_{xy}, d_{x^2-y^2}$) orbitals, then the remaining one

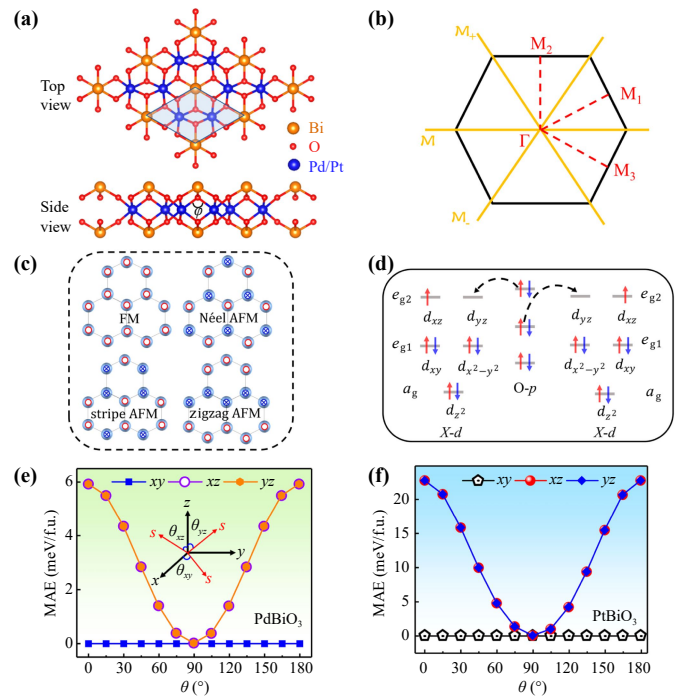


Fig. 1 (a) Crystal structure of ML $X\text{BiO}_3$ ($X = \text{Pd}, \text{Pt}$). The blue region denotes the unit cell. (b) First Brillouin zone with high symmetry points. The three orange lines represent the vertical mirror planes. (c) The FM and three AFM configurations. The magnetization directions of transition metal ion are illustrated by different shapes with two colors. (d) The super-exchange mechanism of $X\text{-O-X}$ in the ML $X\text{BiO}_3$. The variation of MAE for ML (e) PdBiO_3 and (f) PtBiO_3 in xy , xz and yz planes as a function of the magnetization direction angle θ_{xy} , θ_{xz} and θ_{yz} . The inset in (e) illustrates the rotation of the spin vector S by an angle ranging from 0° to 180° .

occupies one of the $e_{\text{g}2}$ (d_{xz}, d_{yz}) orbitals, as shown in Fig. 1(d). This is consistent with the above analysis of the energy difference between FM and AFM configurations, and suggesting a strong and robust FM coupling in the present ML $X\text{BiO}_3$. The FM state is attributed to the Pd(Pt)–O–Pd(Pt) super-exchange interactions, as depicted in Fig. 1(d). The d orbital of X ($X = \text{Pd}, \text{Pt}$) easily hybrids with the p orbital of O, which results in the super-exchange interactions through O atoms. Moreover, the Pd–O–Pd/Pt–O–Pt angle φ is relax to $92.9^\circ/91.4^\circ$, closing to 90° , preferring FM coupling according to Goodenough–Kanamori–Anderson rule [51–53]. As a result, the same d orbitals of two Pd/Pt atoms can only be occupied by the electrons with the same spin state, thereby resulting in FM coupling. Figures S2(c) and (d) present the density of states (DOSs) for ML $X\text{BiO}_3$. The spin-up and spin-down TDOS values of the ML $X\text{BiO}_3$ are not symmetrical, indicating it is FM behavior. From the partial density of states (PDOS) of X atom, it is noted that the d orbital dominates the magnetism of ML $X\text{BiO}_3$, while the Bi

and O atoms do not contribute to the magnetism.

Furthermore, the magnetic anisotropy energy (MAE) of ML $X\text{BiO}_3$ is calculated, which is defined as: $\text{MAE} = E_\theta - E_{[100]}$, where E_θ and $E_{[100]}$ are the total energies of the system with the magnetization along θ and $[100]$ directions, respectively, as shown in the inset of Fig. 1(e) [54, 55]. In xy plane, the MAE is isotropic for different magnetization angle θ_{xy} . However, in xz and yz planes, the MAE varies with the magnetization angles of θ_{xz} and θ_{yz} . Thus, the easy axis of magnetization about ML PdBiO_3 and PtBiO_3 are located at in-plane with a MAE value of 5.09 and 22.8 meV/f.u., respectively, as displayed in Figs. 1(e) and (f). According to the Mermin-Wagner theorem [56], the ML PdBiO_3 and PtBiO_3 should not be magnetically long-range ordered. Therefore, ML $X\text{BiO}_3$ belongs to XY magnets, which would present a Berezinskii–Kosterlitz–Thouless (BKT) transition at the critical temperature T_{BKT} [57, 58]. Based on this theoretical framework, an estimation can be made for T_{BKT} of ML $X\text{BiO}_3$ as $T_{\text{BKT}} = 0.89 J/k_B$ [59, 60], where J represents the exchange integral and k_B denotes the Boltzmann constant. The T_{BKT} values of ML PdBiO_3 and PtBiO_3 are 432 and 550 K, respectively, which are higher than the observation temperature of ML MnBiTe (1.4 K) [61]. Thus, ML PdBiO_3 and PtBiO_3 are promising to be applied in the magnetic electronic devices at room temperature.

Notably, there exist some compounds made of Pd, Pt, Bi and O atoms, which are really existing. Such as the perovskite LaPdO_3 has been synthesized through the high-pressure techniques [62, 63]. The oxidized $\text{Pt}_x\text{Bi}_y\text{O}_z$ cluster is formed via an incipient wetness impregnation [64, 65]. Nanocomposites consisting of 5% Pt supported on activated carbon and promoted with 5% Bi or Sb are prepared by electroless deposition and microwave-assisted methods [66]. More importantly, ML $X\text{BiO}_3$ exhibits the same structure with SrRu_2O_6 , which has been prepared by using low-temperature hydrothermal synthesis and scalable technique of liquid exfoliation [67, 68]. Therefore, ML $X\text{BiO}_3$ can also be obtained from $X\text{Bi}_2\text{O}_6$ in experiment using the aforementioned methods.

3.2 Electric structure and topological property

The energy band of ML $X\text{BiO}_3$ is used to investigate its electronic and spin polarization properties. Figure 2 shows the energy band structure of ML PdBiO_3 . As displayed in Fig. 2(a), without considering SOC effect, the spin-down state behaves as a semiconductor, while the spin-up state exhibits a semimetal state with a Dirac cone crossing the Fermi level. It induces a 100% spin polarization, showing a potential application in spintronics [69, 70]. Notably, due to C_3 rotation symmetry, there are a total of six Dirac cones all over the Brillouin zone, as indicated in Fig. 2(b). As shown in Fig. S3, the Ψ

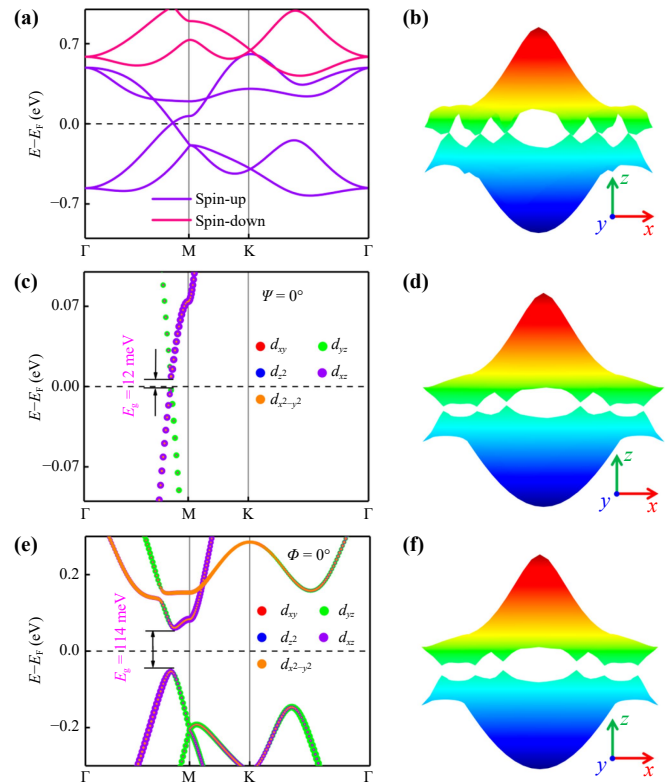


Fig. 2 (a) Spin-resolved and (b) 3D energy bands of ML PdBiO_3 without considering SOC effect. (c) Orbital-resolved and (d) 3D energy bands of ML PdBiO_3 with considering SOC effect as the magnetization direction angle $\Psi = 0^\circ$ in xy plane. (e) Orbital-resolved and (f) 3D energy bands of ML PdBiO_3 with considering SOC effect as the magnetization direction angle $\Phi = 0^\circ$ in xz plane.

and Φ represent the angle between the orientation of magnetization and x direction and the angle between the orientation of magnetization and the z direction, respectively. With considering SOC effect, the Dirac cone is opened as the magnetization direction angle $\Psi = 0^\circ$ in xy plane with a band gap 12 meV, as depicted in Fig. 2(c). Moreover, both the d_{xz} and d_{yz} orbitals simultaneously appears in both conduction and valence bands, meaning energy inversion occurs. It should be noted that all of six Dirac cones are separated, as shown in Fig. 2(d). These indicate that an in-plane QAHE is induced in present ML PdBiO_3 with a topological gap of 12 meV. Unexpected, ML PdBiO_3 also behaves as an out-of-plane QAHE as the magnetization direction angle $\Phi = 0^\circ$ in xz plane, as indicated in Figs. 2(e) and (f). Under this case, the topological gap describes to 114 meV, which exceeds thermal fluctuation energy ~ 25 meV at room temperature. As a result, the topological property of ML PdBiO_3 can be controlled through altering its magnetization direction. Notably, the topological feature of ML PtBiO_3 also varies with the change of magnetization direction, as indicated in Fig. S4. Furthermore, the band structure based on the HSE06

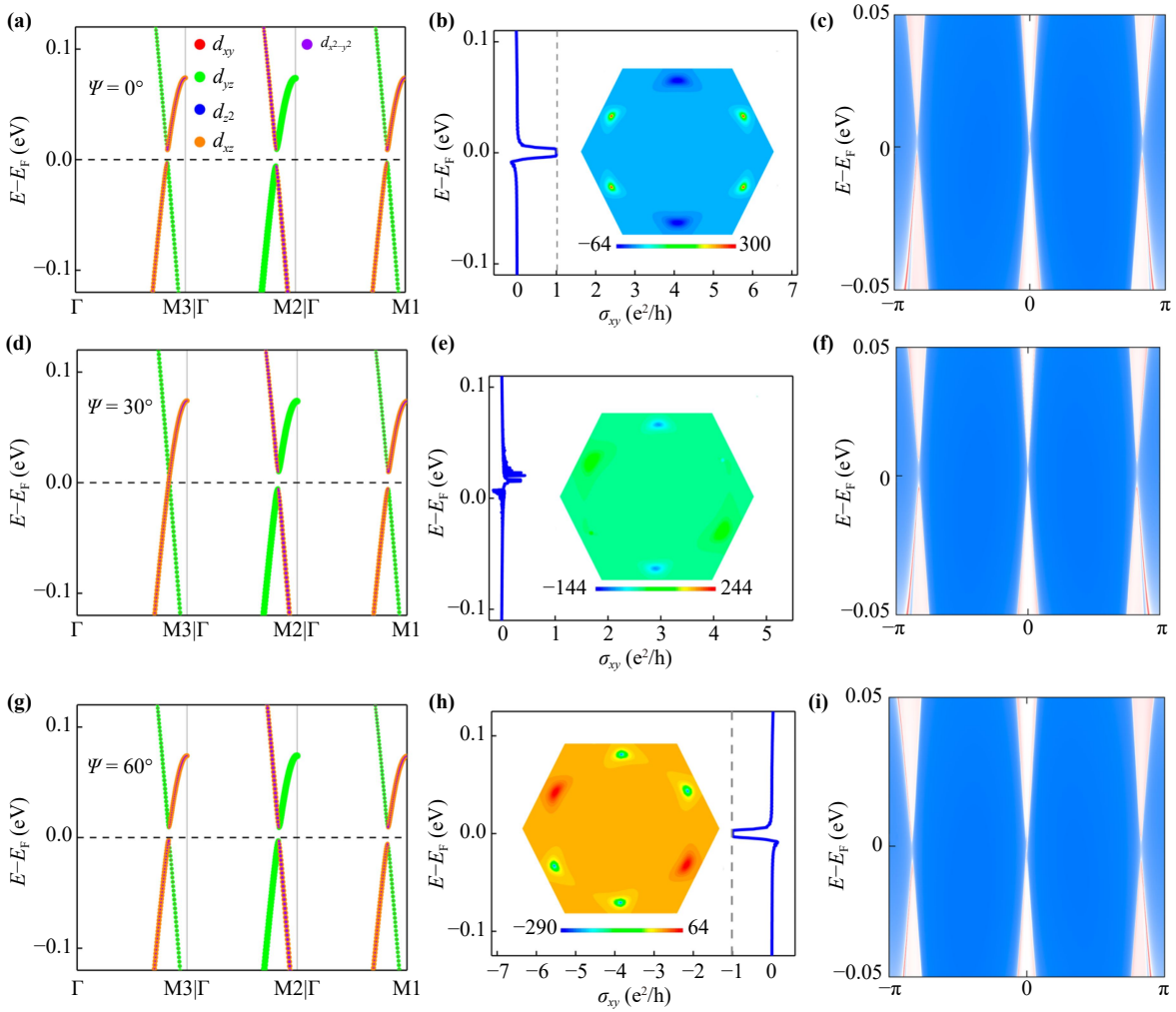


Fig. 3 (a) Orbital-resolved energy band, (b) anomalous Hall conductivity with Berry curvature inset, and (c) chiral edge state of ML PdBiO₃ as the magnetization direction angle $\Psi = 0^\circ$ in xy plane. (d) Orbital-resolved energy band, (e) anomalous Hall conductivity with Berry curvature inset, and (f) chiral edge state as $\Psi = 30^\circ$. (g) Orbital-resolved energy band, (h) anomalous Hall conductivity with Berry curvature inset, and (i) chiral edge state as $\Psi = 60^\circ$.

function is also carried out for comparison. It is found that the HSE06 scheme reveals the same electronic feature as that obtained from the above-mentioned PBE+ U computation, as indicated in Fig. S5. Therefore, the PBE+ U method is reliable and is selected for the present calculations.

The above content indicates that the topological characteristic is directly related with the magnetization direction in ML XBiO₃. Therefore, we furtherly investigate the QAH behavior of ML XBiO₃ under different M direction angles in the xy and xz planes, respectively. Figure 3 shows the topological property of ML PdBiO₃ under different magnetization direction in xy plane. As shown in Fig. 3(a), all three Dirac cones along Γ -M1, Γ -M2 and Γ -M3 high symmetry lines are opened, and energy inversion occurs around the Dirac cones, indicating the QAH behavior in ML PdBiO₃ with $\Psi = 0^\circ$ in xy plane. To further determine the Chern number C , the

corresponding anomalous Hall conductivity (σ_{xy}), Berry curvature ($\Omega_z(\mathbf{k})$) and chiral edge state are further studied, which can be calculated as [71, 72]

$$\sigma_{xy} = -\frac{e^2}{\hbar} \int_{\text{BZ}} \frac{d\mathbf{k}}{(2\pi)^2} \Omega_z(\mathbf{k}) \hbar, \quad (1)$$

$$\Omega_z(\mathbf{k}) = -\sum_n \sum_{n \neq m} f_n(\mathbf{k}) \frac{2\text{Im} \langle \psi_{n\mathbf{k}} | \hat{v}_x | \psi_{m\mathbf{k}} \rangle \langle \psi_{m\mathbf{k}} | \hat{v}_y | \psi_{n\mathbf{k}} \rangle}{(E_{n\mathbf{k}} - E_{m\mathbf{k}})^2}, \quad (2)$$

where e and \hbar are the electronic charge and reduced Planck constant, respectively. The $f_n(\mathbf{k})$ is the Fermi-Dirac distribution function and \mathbf{k} being the electron wave vector, \hat{v}_x is the x component of velocity operator, and $E_{n\mathbf{k}}$ is the eigenvalue of Bloch wave function $\psi_{n\mathbf{k}}$. As shown in Fig. 3(b), the σ_{xy} is calculated as $1 \text{ e}^2/\hbar$

near the Fermi level, indicating a QAHE with $C = 1$. It is caused by one pair of negative extreme Berry curvatures and two pairs of positive Berry curvatures distributed throughout the Brillouin zone, which corresponds to Berry phases of -2π and 4π , respectively, resulting in a total Berry phase of 2π in ML PdBiO₃, being consistent with $C = 1$, as drawn in the insert of Fig. 3(b). This quantum feature is also indicated by the appearing one chiral edge state connecting conduction and valence band along the high symmetry line, as plotted in Fig. 3(c).

As the magnetization direction angle change to $\Psi = 30^\circ$, the Dirac cone along Γ -M3 high symmetry line is closed, while the Dirac cones along Γ -M2 and Γ -M1 high symmetry lines are still open with energy inversion occurs, indicating an intrinsic semimetal state, as shown in Fig. 3(d). It is induced by the protected M_+ and broken M and M_- symmetries under magnetization direction angle $\Psi = 30^\circ$ [48, 73]. The obtained σ_{xy} is $-0.02 e^2/h$, losing the QAHE ($C = 0$). It is caused by one pair of negative extreme Berry curvatures and one pair of positive Berry curvatures distributed throughout the Brillouin zone, which corresponds to Berry phases of -2π and 2π , respectively, resulting in a total Berry phase of 0π in ML PdBiO₃, being consistent with $C = 0$, as drawn in the insert of Fig. 3(e). This intrinsic semimetal feature is also indicated by the zero disappearing chiral edge state, as plotted in Fig. 3(f). For the case of $\Psi = 60^\circ$, the Dirac cone along Γ -M1 high symmetry line is opened again with energy inversion occurs, returning to QAH insulator, as plotted in Fig. 3(g). It is induced by breaking all the M , M_+ and M_- symmetries with $\Psi = 60^\circ$ [48, 73]. At this moment, the σ_{xy} becomes $-1 e^2/h$, demonstrating the QAHE with $C = -1$. It is caused by two pairs of negative extreme Berry curvatures and one pair of positive Berry curvatures distributed throughout the Brillouin zone, which corresponds to Berry phases of -4π and 2π , respectively, resulting in a total Berry phase of -2π in ML PdBiO₃, being consistent with $C = -1$, as drawn in the insert of Fig. 3(h). This intrinsic semimetal feature is also indicated by the appearing one chiral edge state along the high symmetry line, as plotted in Fig. 3(i). As a result, ML PdBiO₃ will vary among QAHE with $C = 1$, topological trivial semimetal state and QAHE with $C = -1$ three topological phases with a period of 60° as the magnetization direction angle Ψ various in xy plane, as indicated by Fig. S6.

We also study the QAH behavior of ML PdBiO₃ under different magnetization direction angles Φ in the xz plane. As shown in Fig. 4(a), all three Dirac cones along Γ -M1, Γ -M2 and Γ -M3 high symmetry lines are opened, and energy inversion occurs around the Dirac cones, indicating the topological feature of ML PdBiO₃ with $\Phi = 0^\circ$. As shown in Fig. 4(b), the σ_{xy} is calculated as $3 e^2/h$ near the Fermi level, indicating a QAHE with $C = 3$. It is caused by three pairs of positive extreme

Berry curvatures distributed throughout the Brillouin zone, which result in a total Berry phase of 6π , corresponding to $C = 3$, as drawn in the insert of Fig. 4(b). This quantum characteristic is also indicated by the appearing three chiral edge state connecting conduction and valence band along the high symmetry lines, as plotted in Fig. 4(c). As the magnetization direction angle change to $\Phi = 97.5^\circ$, the Dirac cones along Γ -M1 and Γ -M3 high symmetry lines are still opened, while the Dirac cone along Γ -M2 high symmetry line is closed with energy inversion occurs, as shown in Fig. 4(d). Under this case, ML PdBiO₃ presents a mixed state of intrinsic semimetal and QAH insulator. The calculated σ_{xy} is $-2 e^2/h$, which is contributed by the anomalous Hall conductance of semimetal and QAH states. The QAH state is proven by the two pairs of negative extreme Berry curvature throughout the Brillouin zone, as shown in Fig. 4(e). It is consistent with the appearing two chiral edge state along the high symmetry line, as plotted in Fig. 4(f). Notably, this mixed state of intrinsic semimetal and QAH insulator is also indicated in ML PdBiO₃ with $\Phi = 86.5^\circ$, as shown in Fig. S7(d). For the case of $\Phi = 150^\circ$, all three Dirac cones along Γ -M1, Γ -M2 and Γ -M3 high symmetry lines are opened, ML PdBiO₃ behaves as a QAH insulator with a Chern number $C = -3$, as indicated in Figs. 4(g)–(i). Under $0^\circ - 86.5^\circ$, ML PdBiO₃ behaves as an QAH insulators with $C = 3$, as indicate in Fig. S7. Comparatively, under $-86.5^\circ - 97.5^\circ$, presents an QAH states with $C = 1$. As a result, ML PdBiO₃ will vary among QAHE with $C = |3|$, intrinsic semimetal state and QAHE with $C = |1|$ three topological phases as the magnetization direction angle Φ various in xz plane. Notably, this topological phase transition behavior depending on magnetization direction is also observed in PtBiO₃, as indicated in Fig. S8.

The magnetic and electric properties of 2D magnetic materials with transition metal elements is related to the electronic correlation strength of the system, which is affected by the strain and U value [74, 75]. Therefore, the topological characteristic of ML XBiO₃ under different strain and U values are studied. The strain can be defined as $\varepsilon = (\alpha - \alpha_0)/\alpha_0$ [76, 77], where α_0 and α are lattice constants of ML XBiO₃ without and with strain, respectively. As shown in Fig. 5(a), the energy difference (ΔE) between AFM and FM states increases gradually from -3% to 3% strains. Moreover, ΔE is always positive during the entire range of strains, indicating a FM coupling of ML XBiO₃. As described in Fig. 5(b), the MAE also decreases from -3% to 3% strains, and keep a positive value, keeping an in-plane magnetic anisotropy. Furthermore, during the strain progress, the topological band gap of ML XBiO₃ gradually decreases, as plotted in Fig. 5(c) and Fig. S9(a). Under $0-5 U$ values, the ΔE enlarge gradually with positive values and MAE reduce gradually with positive values, demonstrating a FM coupling and an in-plane magnetic anisotropy of ML

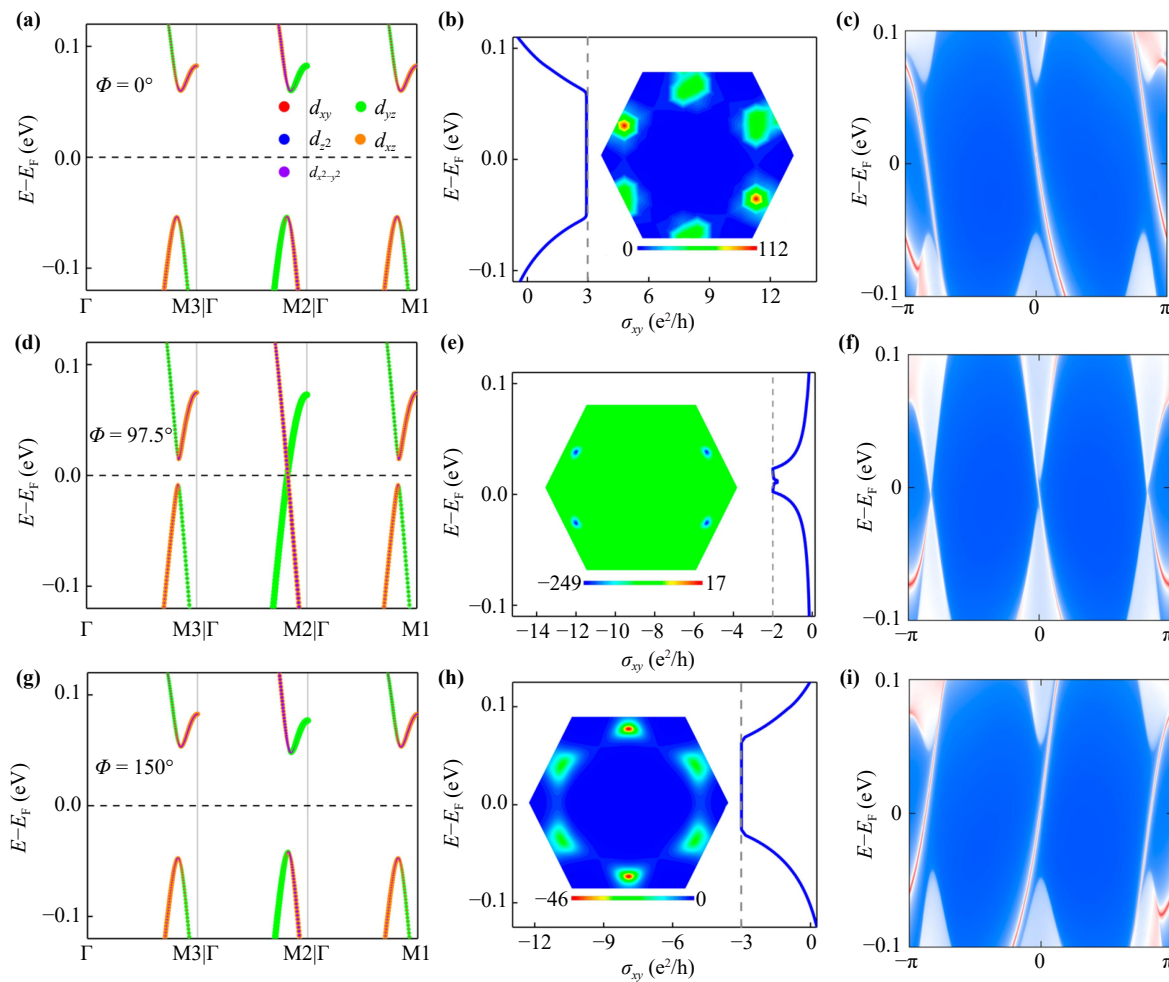


Fig. 4 (a) Orbital-resolved energy band, (b) anomalous Hall conductivity with Berry curvature inset, and (c) chiral edge state of ML PdBiO₃ as the magnetization direction angle $\Phi = 0^\circ$ in xz plane. (d) Orbital-resolved energy band, (e) anomalous Hall conductivity with Berry curvature inset, and (f) chiral edge state as $\Phi = 97.5^\circ$. (g) Orbital-resolved energy band, (h) anomalous Hall conductivity with Berry curvature inset, and (i) chiral edge state as $\Phi = 150^\circ$.

XBiO₃, as described in Figs. 5(d) and (e). Moreover, throughout the U values, ML XBiO₃ also keeps a QAHE, and the topological gap decreases gradually with the increases of U value, as indicated in Fig. 5(f) and Fig. S9(b). The various U values would change the electronic correlation strength for ML XBiO₃ ($X = \text{Pd}, \text{Pt}$) [61, 78, 79]. In a word, the QAHE of ML XBiO₃ is robust for strain and U value. It has been established that the growth of materials on specific substrates inherently gives rise to strain [80]. For illustration, we construct a XBiO₃-MoS₂ heterostructure (1×1 XBiO₃ and $\sqrt{3} \times \sqrt{3}$ MoS₂), in which the ML XBiO₃ is above the ML MoS₂ (see Fig. S10). After the structural relaxation, the in-plane lattice constants of ML PdBiO₃ and PtBiO₃ are enlarged by 1.3% and 0.3%, respectively.

Figure 6(a) shows the schematic of the QAHE measurement by varying the orientation of magnetization. Under the action of in-plane electric field, the transverse voltage (conductivity) can be detected by the

regulating the magnetization of Pd/Pt atoms in ML XBiO₃ in xy and xz planes using an external magnetic field. The detected platformized conductivity indicates the QAH state of ML XBiO₃. Figure 6(b) displays the topological phases of ML XBiO₃. It can be found that ML XBiO₃ changes among QAHE with $C = |3|$, QAHE with $C = |1|$ and topologically trivial semimetal state for different magnetization directions. Based on these analysis and above research results, the variation of Chern number and topological band gap of ML XBiO₃ with the magnetization direction can be obtained. As shown in Fig. 6(c), when magnetization direction angle Ψ varying in the xy plane, the Chern number alternatively changes between $C = 1$ and $C = -1$ with a period of 60° . Moreover, as $\Psi = 30^\circ, 90^\circ, 150^\circ, 210^\circ, 270^\circ$ and 330° , ML XBiO₃ presents a semimetal state. As shown in Fig. 6(d), ML XBiO₃ presents a Chern number of 3 and -3 as Φ located in the range of 277.5° – 86.5° and 97.5° – 266.5° , respectively. Furthermore, ML PdBiO₃

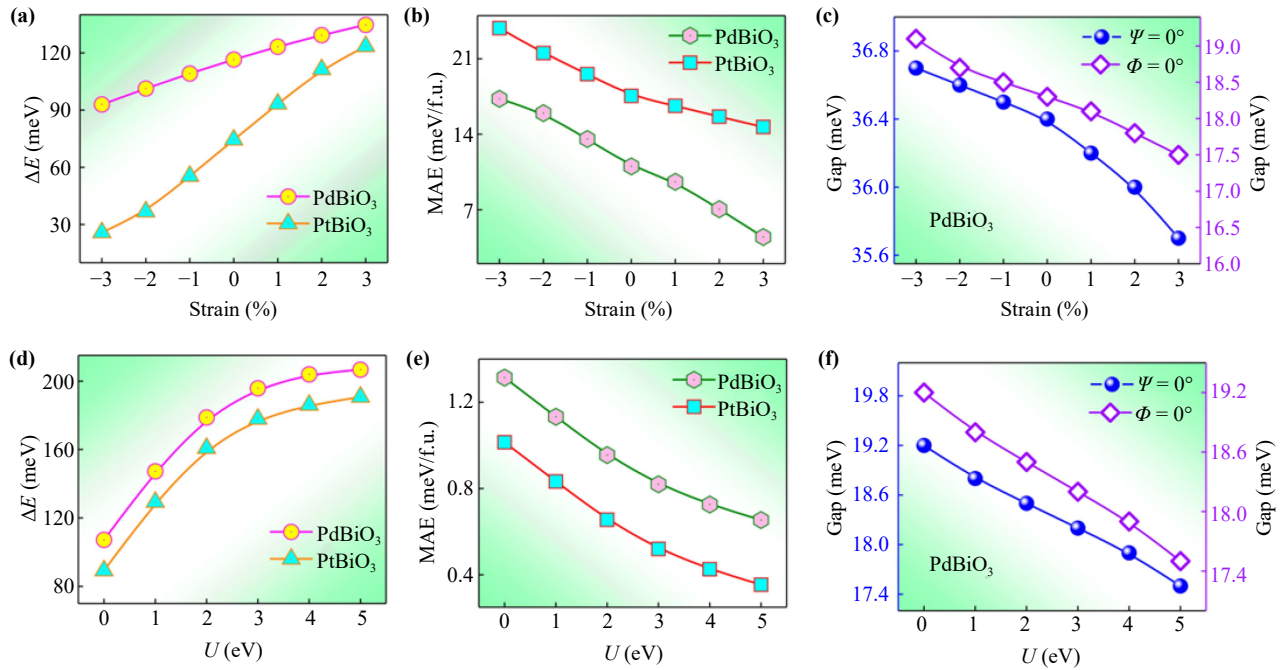


Fig. 5 (a) Energy difference (ΔE) between AFM and FM states and (b) MAE with magnetization direction angles $\Psi = 0^\circ$ and $\Phi = 0^\circ$ of ML XBiO_3 under different strains. (d) ΔE between AFM and FM states and (e) MAE with magnetization direction angles $\Psi = 0^\circ$ and $\Phi = 0^\circ$ of ML XBiO_3 under different U values. The topological gaps with magnetization direction angles $\Psi = 0^\circ$ and $\Phi = 0^\circ$ of ML PdBiO_3 (c) under different strains and (f) under different U values.

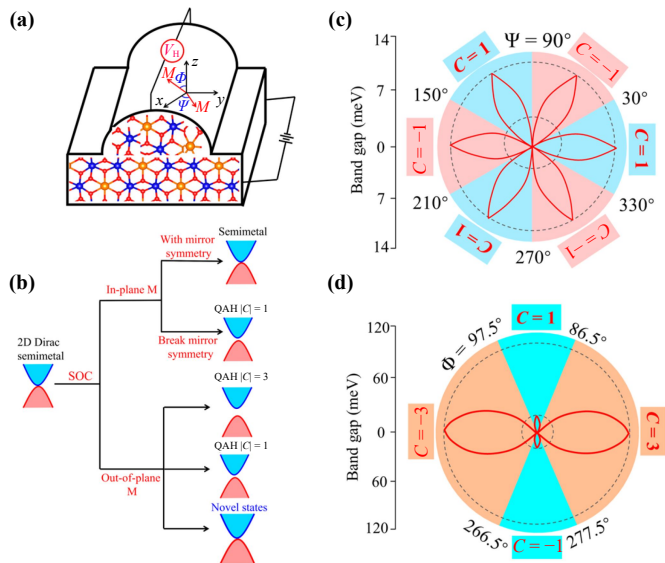


Fig. 6 (a) Schematic of the QAHE measurement by varying the orientation of magnetization. (b) Different topological phases realized in the ML XBiO_3 . (c) Phase diagram of Chern number as a function of magnetization direction angles Ψ in xy plane. (d) Phase diagram of Chern number as a function of magnetization direction angles Φ in xz plane. The polar radius indicates the value of band gap.

presents a Chern number of 1 and -1 as Φ located in the range of 86.5° – 97.5° and 266.5° – 277.5° , respectively. Under $\Phi = 86.5^\circ$, 97.5° , 266.5° and 277.5° , ML XBiO_3

behave as a mixed state of semimetal and QAH state. As a result, the Chern number of ML PdBiO_3 can be regulated by controlling the magnetization direction, which provides an example for tuning the Chern number of QAH insulators.

4 Conclusion

In conclusion, the magnetic properties, electronic structures, and topological characteristics of monolayer XBiO_3 ($X = \text{Pd}, \text{Pt}$) are studied through the first-principles calculations. The monolayer XBiO_3 present ferromagnetic ground states with in-plane magnetic anisotropy. The critical magnetic transition temperature of monolayers PdBiO_3 and PtBiO_3 reach up to 432 and 550 K, respectively. The magnetic coupling feature of monolayer XBiO_3 are induced by the super-exchange interaction along $X\text{-O-X}$ path. Interestingly, monolayer XBiO_3 can exhibit QAHE with tunable Chern number. When the magnetization direction changes in the xy plane, monolayer XBiO_3 switch between QAH insulator with $C = |1|$ and topological trivial semimetal with a period of 60° . It is caused by the breaking or protecting mirror symmetries for different polar angle Ψ . Comparatively, as the magnetization direction alters in the xz plane, monolayer XBiO_3 vary among QAH insulator with $C = |3|$, QAH insulator with $C = |1|$ as well as mixed semimetal and QAH state with a period of 180° .



Therefore, the Chern number of monolayer $X\text{BiO}_3$ can be regulated by adjusting the magnetization direction. The topological band gap is as high as 114 and 132 meV for monolayers PdBiO_3 and PtBiO_3 , respectively, matching with $C = \pm 3$. Notably, under -3% to 3% strains or $0-5$ eV U values, QAHE keeps stable for the present systems. Our work provides an ideal platform to investigate the tunable high Chern number QAHE.

Declarations The authors declare no competing financial interest.

Electronic supplementary materials The online version contains supplementary material available at <https://doi.org/10.15302/front-phys.2026.015201>.

Acknowledgements This work was supported by the National Natural Science Foundation of China (Nos. 52271238, 12261131506, and 12074052), the Liaoning Revitalization Talents Program (No. XLYC2002075), the Natural Science Foundation of Liaoning Province of China (No. 2021-YQ-06), and the Research Funds for the Central Universities (No. N2402002).

References

- J. Wang, A. Khosravi, A. Vanossi, and E. Tosatti, Colloquium: Sliding and pinning in structurally lubric 2D material interfaces, *Rev. Mod. Phys.* 96(1), 011002 (2024)
- N. Morales-Durán, J. T. Shi, and A. H. MacDonald, Fractionalized electrons in moiré materials, *Nat. Rev. Phys.* 6(6), 349 (2024)
- A. J. Yang, S. X. Wang, J. W. Xu, X. J. Loh, Q. Zhu, and X. R. Wang, Two-dimensional layered materials meet perovskite oxides: A combination for high performance electronic devices, *ACS Nano* 17(11), 9748 (2023)
- Z. Liu, L. J. Deng, and B. Peng, Ferromagnetic and ferroelectric two-dimensional materials for memory application, *Nano Res.* 14(6), 1802 (2021)
- M. Wu, Z. L. Li, T. Cao, and S. G. Louie, Physical origin of giant excitonic and magnetooptical responses in two-dimensional ferromagnetic insulators, *Nat. Commun.* 10(1), 2371 (2019)
- P. Li, X. Li, W. Zhao, H. Chen, M. X. Chen, Z. X. Guo, J. Feng, X. G. Gong, and A. H. MacDonald, Topological Dirac states beyond π -orbitals for silicene on $\text{SiC}(0001)$ surface, *Nano Lett.* 17(10), 6195 (2017)
- T. Zhong, X. Li, M. Wu, and J. M. Liu, Room-temperature multiferroicity and diversified magnetoelectric couplings in 2D materials, *Natl. Sci. Rev.* 7(2), 373 (2020)
- H. Y. Ma, M. Hu, N. Li, J. Liu, W. Yao, J. F. Jia, and J. Liu, Multifunctional antiferromagnetic materials with giant piezomagnetism and noncollinear spin current, *Nat. Commun.* 12(1), 2846 (2021)
- W. Y. Tong, S. J. Gong, X. Wan, and C. G. Duan, Concepts of ferrovalley material and anomalous valley Hall effect, *Nat. Commun.* 7(1), 13612 (2016)
- T. Zhang, X. Xu, B. Huang, Y. Dai, L. Kou, and Y. Ma, Layer-polarized anomalous Hall effects in valleytronic van der Waals bilayers, *Mater. Horiz.* 10(2), 483 (2023)
- W. Ding, J. Zeng, W. Qin, P. Cui, and Z. Zhang, Exploring high transition temperature superconductivity in a freestanding or SrTiO_3 -supported CoSb monolayer, *Phys. Rev. Lett.* 124(2), 027002 (2020)
- C. Z. Chang, J. Zhang, X. Feng, J. Shen, Z. Zhang, M. Guo, K. Li, Y. Ou, P. Wei, L. L. Wang, Z. Q. Ji, Y. Feng, S. Ji, X. Chen, J. Jia, X. Dai, Z. Fang, S. C. Zhang, K. He, Y. Y. Wang, L. Lu, X. C. Ma, and Q. K. Xue, Experimental observation of the quantum anomalous Hall effect in a magnetic topological insulator, *Science* 340(6129), 167 (2013)
- M. M. Otrokov, T. V. Menshchikova, M. G. Vergniory, I. P. Rusinov, A. Y. Vyazovskaya, Y. M. Koroteev, G. Bihlmayer, A. Ernst, P. M. Echenique, A. Arnau, and E. V. Chulkov, Highly-ordered wide bandgap materials for quantized anomalous Hall and magnetoelectric effects, *2D Mater.* 4, 025082 (2017)
- M. M. Otrokov, I. I. Klimovskikh, H. Bentmann, D. Estyunin, A. Zeugner, et al., Prediction and observation of an antiferromagnetic topological insulator, *Nature* 576(7787), 416 (2019)
- Y. J. Deng, Y. J. Yu, M. Z. Shi, Z. X. Guo, Z. H. Xu, J. Wang, X. H. Chen, and Y. B. Zhang, Quantum anomalous Hall effect in intrinsic magnetic topological insulator MnBi_2Te_4 , *Science* 367(6480), 895 (2020)
- Y. Wu, L. Deng, J. Tong, X. Yin, G. Qin, and X. Zhang, Layer-dependent quantum anomalous Hall and quantum spin Hall effects in two-dimensional LiFeTe , *ACS Appl. Mater. Interfaces* 16(31), 41371 (2024)
- Y. T. Liu and Q. M. Shao, Two-dimensional materials for energy-efficient spin-orbit torque devices, *ACS Nano* 14(8), 9389 (2020)
- M. Blei, J. L. Lado, Q. Song, D. Dey, O. Erten, V. Pardo, R. Comin, S. Tongay, and A. S. Botana, Synthesis, engineering, and theory of 2D van der Waals magnets, *Appl. Phys. Rev.* 8(2), 021301 (2021)
- P. Ritzinger and K. Výborný, Anisotropic magnetoresistance: materials, models and applications, *R. Soc. Open Sci.* 10(10), 230564 (2023)
- R. Peng, Y. D. Ma, X. L. Xu, Z. L. He, B. B. Huang, and Y. Dai, Intrinsic anomalous valley Hall effect in single-layer Nb_3I_8 , *Phys. Rev. B* 102(3), 035412 (2020)
- Y. Wu, J. Tong, L. Deng, F. Luo, F. Tian, G. Qin, and X. Zhang, Realizing spontaneous valley polarization and topological phase transitions in monolayer ScX_2 ($X = \text{Cl}, \text{Br}, \text{I}$), *Acta Mater.* 246, 118731 (2023)
- H. Sun, S. S. Li, W. X. Ji, and C. W. Zhang, Valley-dependent topological phase transition and quantum anomalous valley Hall effect in single-layer RuClBr , *Phys. Rev. B* 105(19), 195112 (2022)
- K. Wang, Y. H. Li, H. L. Mei, P. Li, and Z. X. Guo, Quantum anomalous Hall and valley quantum anomalous Hall effects in two-dimensional d^0 orbital XY monolayers, *Phys. Rev. Mater.* 6(4), 044202 (2022)
- P. Li, X. Yang, Q. S. Jiang, Y. Z. Wu, and W. Xun, Built-in electric field and strain tunable valley-related multiple topological phase transitions in VSiXN_4 ($X = \text{C}, \text{Si}, \text{Ge}, \text{Sn}, \text{Pb}$) monolayers, *Phys. Rev. Mater.* 7(6),

- 064002 (2023)
25. S. Y. Pan, Z. Y. Li, and Y. L. Han, Electric-field-tunable topological phases in valley-polarized quantum anomalous Hall systems with inequivalent exchange fields, *Front. Phys. (Beijing)* 20(1), 014207 (2025)
 26. Y. Li, J. Li, Y. Li, M. Ye, F. Zheng, Z. Zhang, J. Fu, W. Duan, and Y. Xu, High-temperature quantum anomalous Hall insulators in lithium-decorated iron-based superconductor materials, *Phys. Rev. Lett.* 125(8), 086401 (2020)
 27. P. H. Jiang, L. Li, Z. L. Liao, Y. X. Zhao, and Z. C. Zhong, Spin direction-controlled electronic band structure in two-dimensional ferromagnetic CrI₃, *Nano Lett.* 18(6), 3844 (2018)
 28. H. Huan, Y. Xue, B. Zhao, H. R. Bao, L. Liu, and Z. Q. Yang, Tunable Weyl half-semimetals in two-dimensional iron-based materials MFeSe ($M = \text{Tl, In, Ga}$), *Phys. Rev. B* 106(12), 125404 (2022)
 29. Z. Y. Li, Y. L. Han, and Z. H. Qiao, Chern number tunable quantum anomalous Hall effect in monolayer transitional metal oxides via manipulating magnetization orientation, *Phys. Rev. Lett.* 129(3), 036801 (2022)
 30. L. Jin, L. R. Wang, X. M. Zhang, Y. Liu, X. F. Dai, H. L. Gao, and G. D. Liu, Fully spin-polarized Weyl fermions and in/out-of-plane quantum anomalous Hall effects in a two-dimensional d^0 ferromagnet, *Nanoscale* 13(11), 5901 (2021)
 31. S. S. Li, X. Y. Li, W. X. Ji, P. Li, S. S. Yan, and C. W. Zhang, Quantum anomalous Hall effect with a high and tunable Chern number in monolayer NdN₂, *Phys. Chem. Chem. Phys.* 25(27), 18275 (2023)
 32. J. Y. You, C. Chen, Z. Zhang, X. L. Sheng, S. A. Yang, and G. Su, Two-dimensional Weyl half-semimetal and tunable quantum anomalous Hall effect, *Phys. Rev. B* 100(6), 064408 (2019)
 33. Y. W. Yu, X. Chen, X. X. Liu, J. Li, B. Sanyal, X. R. Kong, F. M. Peeters, and L. Y. Li, Ferromagnetism with in-plane magnetization, Dirac spin-gapless semiconducting properties, and tunable topological states in two-dimensional rare-earth metal dinitrides, *Phys. Rev. B* 105(2), 024407 (2022)
 34. K. E. Huang, L. Li, W. Zhao, and X. W. Wang, Quantum anomalous Hall effect in monolayers Ti₂X₂ ($X = \text{P, As, Sb, Bi}$) with tunable Chern numbers by adjusting magnetization orientation, *Front. Phys. (Beijing)* 20(2), 024203 (2025)
 35. S. J. Zhang, C. W. Zhang, S. F. Zhang, W. X. Ji, P. Li, P. J. Wang, S. S. Li, and S. S. Yan, Intrinsic Dirac half-metal and quantum anomalous Hall phase in a hexagonal metal-oxide lattice, *Phys. Rev. B* 96(20), 205433 (2017)
 36. B. Wu, Y. L. Song, W. X. Ji, P. J. Wang, S. F. Zhang, and C. W. Zhang, Quantum anomalous Hall effect in an antiferromagnetic monolayer of MoO, *Phys. Rev. B* 107(21), 214419 (2023)
 37. H. S. Lu and G. Y. Guo, Strain and onsite-correlation tunable quantum anomalous Hall phases in ferromagnetic (111) LaXO₃ bilayers ($X = \text{Pd, Pt}$), *Phys. Rev. B* 99(10), 104405 (2019)
 38. G. Kresse and J. Furthmüller, Efficient iterative schemes for *ab initio* total-energy calculations using a plane-wave basis set, *Phys. Rev. B* 54(16), 11169 (1996)
 39. G. Kresse and D. Joubert, From ultrasoft pseudopotentials to the projector augmented-wave method, *Phys. Rev. B* 59(3), 1758 (1999)
 40. J. P. Perdew, K. Burke, and M. Ernzerhof, Generalized gradient approximation made simple, *Phys. Rev. Lett.* 78, 1396 (1996)
 41. S. L. Dudarev, G. A. Botton, S. Y. Savrasov, C. J. Humphreys, and A. P. Sutton, Electron-energy-loss spectra and the structural stability of nickel oxide: An LSDA+*U* study, *Phys. Rev. B* 57(3), 1505 (1998)
 42. X. Gonze and C. Lee, Dynamical matrices, Born effective charges, dielectric permittivity tensors, and interatomic force constants from density-functional perturbation theory, *Phys. Rev. B* 55(16), 10355 (1997)
 43. H. Huan, Y. Xue, B. Zhao, G. Y. Gao, H. R. Bao, and Z. Q. Yang, Strain-induced half-valley metals and topological phase transitions in MBr₂ monolayers ($M = \text{Ru, Os}$), *Phys. Rev. B* 104(16), 165427 (2021)
 44. V. Wang, N. Xu, J. C. Liu, G. Tang, and W. T. Geng, VASPKIT: A user-friendly interface facilitating high-throughput computing and analysis using VASP code, *Comput. Phys. Commun.* 267, 108033 (2021)
 45. A. A. Mostofi, J. R. Yates, G. Pizzi, Y. S. Lee, I. Souza, D. Vanderbilt, and N. Marzari, An updated version of Wannier90: A tool for obtaining maximally-localised Wannier functions, *Comput. Phys. Commun.* 185(8), 2309 (2014)
 46. Q. Wu, S. Zhang, H. F. Song, M. Troyer, and A. A. Soluyanov, WannierTools: An open-source software package for novel topological materials, *Comput. Phys. Commun.* 224, 405 (2018)
 47. H. J. Lian, X. K. Xu, J. L. Lu, X. J. Yao, A. L. He, and X. Y. Zhang, Quantum anomalous Hall states in Li/Nadoped Kagome V₃X₈ ($X = \text{Cl, Br}$) monolayers, *J. Alloys Compd.* 1017, 179103 (2025)
 48. X. Y. Xuan, Z. H. Zhang, C. F. Chen, and W. L. Guo, Robust quantum anomalous Hall states in monolayer and few layer TiTe, *Nano Lett.* 22(13), 5379 (2022)
 49. K. Junjuro, Superexchange interaction and symmetry properties of electron orbitals, *J. Phys. Chem. Solids* 10(2-3), 87 (1959)
 50. H. Chen, J. Lu, N. Wang, X. Zha, G. Hu, X. Yuan, and J. Ren, Strain-induced high-Chern-number spin-unlocked edge states in monolayer MnAsO₃ with intrinsic quantum anomalous Hall effect, *Appl. Phys. Lett.* 124(15), 153101 (2024)
 51. P. W. Anderson, New approach to the theory of superexchange interactions, *Phys. Rev.* 115(1), 2 (1959)
 52. J. B. Goodenough, Theory of the role of covalence in the perovskite-type manganites [La, M(II)]MnO₃, *Phys. Rev.* 100(2), 564 (1955)
 53. J. Kanamori, Crystal distortion in magnetic compounds, *J. Appl. Phys.* 31(5), S14 (1960)
 54. X. Cheng, S. Xu, F. Jia, G. Zhao, M. Hu, W. Wu, and W. Ren, Intrinsic ferromagnetism with high Curie temperature and strong anisotropy in a ferroelastic VX monolayer ($X = \text{P, As}$), *Phys. Rev. B* 104(10), 104417 (2021)
 55. A. N. Ma, P. J. Wang, and C. W. Zhang, Intrinsic ferromagnetism with high temperature, strong anisotropy and controllable magnetization in the CrX



- ($X = \text{P, As}$) monolayer, *Nanoscale* 12(9), 5464 (2020)
56. N. D. Mermin and H. Wagner, Absence of ferromagnetism or antiferromagnetism in one- or two-dimensional isotropic Heisenberg models, *Phys. Rev. Lett.* 17(22), 1133 (1966)
 57. S. Zhang, R. Xu, W. Duan, and X. Zou, Intrinsic halfmetallicity in 2D ternary chalcogenides with high critical temperature and controllable magnetization direction, *Adv. Funct. Mater.* 29(14), 1808380 (2019)
 58. K. Sheng, H. K. Yuan, and B. Zhang, Intrinsic spin, valley and piezoelectric polarizations in room-temperature ferrovalley Janus TiXY ($\text{XY} = \text{SCl}$ and SeBr) monolayers, *Nanoscale* 14(40), 15156 (2022)
 59. J. F. Fernández, M. F. Ferreira, and J. Stankiewicz, Critical behavior of the two-dimensional XY model: A Monte Carlo simulation, *Phys. Rev. B* 34(1), 292 (1986)
 60. H. L. Zhuang and R. G. Hennig, Stability and magnetism of strongly correlated single-layer VS_2 , *Phys. Rev. B* 93(5), 054429 (2016)
 61. M. Serlin, C. L. Tschirhart, H. Polshyn, Y. Zhang, J. Zhu, K. Watanabe, T. Taniguchi, L. Balents, and A. F. Young, Intrinsic quantized anomalous Hall effect in a moiré heterostructure, *Science* 367(6480), 900 (2020)
 62. S. J. Kim, S. Lemaux, G. Demazeau, J. Y. Kim, and J. H. Choy, LaPdO_3 : The First Pd^{III} Oxide with the Perovskite Structure, *J. Am. Chem. Soc.* 123(42), 10413 (2001)
 63. S. J. Kim, S. Lemaux, G. Demazeau, J. Y. Kim, and J. H. Choy, X-ray absorption spectroscopic study on LaPdO_3 , *J. Mater. Chem.* 12(4), 995 (2002)
 64. B. Nan, Q. Fu, J. Yu, M. Shu, L. L. Zhou, J. Y. Li, W. W. Wang, C. J. Jia, C. Ma, J. X. Chen, L. N. Li, and R. Si, Unique structure of active platinum-bismuth site for oxidation of carbon monoxide, *Nat. Commun.* 12(1), 3342 (2021)
 65. B. Nan, L. L. Li, Y. N. Li, L. L. Guo, M. Du, Z. W. Liu, X. Tao, C. Tian, Z. Y. Liang, Y. X. Zhang, C. Ma, L. Shen, R. Si, and L. N. Li, Hydrogen-controlled structural reconstruction of palladium-bismuth oxide cluster to single atom alloy for low-temperature CO oxidation, *Appl. Catal. B* 334, 122818 (2023)
 66. M. V. Maphoru, S. K. Pillai, and J. Heveling, Structure-activity relationships of carbon-supported platinum-bismuth and platinum-antimony oxidation catalysts, *J. Catal.* 348, 47 (2017)
 67. C. I. Hiley, M. R. Lees, J. M. Fisher, D. Thompsett, S. Agrestini, R. I. Smith, and R. I. Walton, Ruthenium(V) oxides from low-temperature hydrothermal synthesis, *Angew. Chem. Int. Ed.* 53(17), 4423 (2014)
 68. S. Homkar, B. Chand, S. S. Rajput, S. Gorantla, T. Das, R. Babar, S. Patil, R. Klingeler, S. Nair, M. Kabir, and A. Bajpai, Few-layer SrRu_2O_6 nanosheets as non-van der Waals honeycomb antiferromagnets: Implications for two dimensional spintronics, *ACS Appl. Nano Mater.* 4(9), 9313 (2021)
 69. W. E. Pickett and J. S. Moodera, Half metallic magnets, *Phys. Today* 54(5), 39 (2001)
 70. I. Žutić, J. Fabian, and S. D. Sarma, Spintronics: Fundamentals and applications, *Rev. Mod. Phys.* 76, 323 (2004)
 71. D. J. Thouless, M. Kohmoto, M. P. Nightingale, and M. Den-Nijs, Quantized Hall conductance in a two-dimensional periodic potential, *Phys. Rev. Lett.* 49(6), 405 (1982)
 72. K. Sheng, Q. Chen, H. K. Yuan, and Z. Y. Wang, Monolayer CeI_2 : An intrinsic room-temperature ferrovalley semiconductor, *Phys. Rev. B* 105(7), 075304 (2022)
 73. J. Wang, B. Lian, H. J. Zhang, Y. Xu, and S. C. Zhang, Quantum anomalous Hall effect with higher plateaus, *Phys. Rev. Lett.* 111(13), 136801 (2013)
 74. S. D. Guo, J. X. Zhu, M. Y. Yin, and B. G. Liu, Substantial electronic correlation effects on the electronic properties in a Janus FeClF monolayer, *Phys. Rev. B* 105(10), 104416 (2022)
 75. K. Jia, X. J. Dong, S. S. Li, W. X. Ji, and C. W. Zhang, First-principles study reveals an electronic correlation effect on the topological and electronic properties of Janus RuClF monolayers: Implications for spintronics and valleytronics applications, *ACS Appl. Nano Mater.* 6(15), 14003 (2023)
 76. Z. W. Li, Y. W. Lv, L. W. Ren, J. Li, L. G. Kong, Y. J. Zeng, Q. Y. Tao, R. X. Wu, H. F. Ma, B. Zhao, D. Wang, W. Q. Dang, K. Q. Chen, L. Liao, X. D. Duan, X. F. Duan, and Y. Liu, Efficient strain modulation of 2D materials via polymer encapsulation, *Nat. Commun.* 11(1), 1151 (2020)
 77. Z. H. Dai, L. Q. Liu, and Z. Zhang, Strain engineering of 2D materials: Issues and opportunities at the interface, *Adv. Mater.* 31(45), 1805417 (2019)
 78. Y. Cao, D. Rodan-Legrain, O. Rubies-Bigorda, J. M. Park, K. Watanabe, T. Taniguchi, and P. Jarillo-Herrero, Tunable correlated states and spin-polarized phases in twisted bilayer-bilayer graphene, *Nature* 583(7815), 215 (2020)
 79. P. Stepanov, I. Das, X. B. Lu, A. Fahimniya, K. Watanabe, T. Taniguchi, F. H. L. Koppens, J. Lischner, L. Levitov, and D. K. Efetov, Untying the insulating and superconducting orders in magic-angle graphene, *Nature* 583(7816), 375 (2020)
 80. C. D. Zhang, M. Y. Li, J. Tersoff, Y. M. Han, Y. S. Su, L. J. Li, D. A. Muller, and C. K. Shih, Strain distributions and their influence on electronic structures of WSe_2 - MoS_2 laterally strained heterojunctions, *Nat. Nanotechnol.* 13(2), 152 (2018)